

# Solvent Co-Intercalation-Induced Activation and Capacity Fade Mechanism of Few-/Multi-Layered MXenes in Lithium Ion Batteries

Peer Bärmann,\* Martin Winter, Jesus Gonzalez-Julian, and Tobias Placke\*

MXenes attract tremendous research efforts since their discovery in 2011 due to their unique physical and chemical properties, allowing for application in various fields. One of them is electrochemical energy storage due to their pseudocapacitive (=redox) behavior, high electronic conductivity, and charge storage versatility regarding the cationic species (e.g., Li<sup>+</sup>). MXenes typically display stable charge/discharge cycling behavior over hundreds of cycles in numerous electrolytes, however, a drastic loss of reversible capacity is detectable during the initial cycles. Furthermore, an electrochemical "activation" is also reported in the literature, especially for free-standing electrodes. Here, these electrochemical phenomena are investigated by electrochemical and analytical means to decipher the responsible mechanism by comparing few-layered and multilayered Ti<sub>3</sub>C<sub>2</sub>T<sub>x</sub>. A change in the pseudocapacitive behavior of MXenes during cycling can be explained by in situ X-ray diffraction studies, revealing solvent co-intercalation in the first cycle for the morphologically different MXenes. This co-intercalation is responsible for the capacity decay detected in the first cycles and is also responsible for the ongoing "activation" occurring in later cycles.

1. Introduction

The term MXenes describes an expanding group of 2D layered transition metal carbides and nitrides that are found to

P. Bärmann, M. Winter, T. Placke University of Münster MEET Battery Research Center Institute of Physical Chemistry

Corrensstr. 46, 48149 Münster, Germany

E-mail: baermann@wwu.de; tobias.placke@uni-muenster.de

M. Winter

Helmholtz Institute Münster

IEK-12

Forschungszentrum Jülich GmbH Corrensstr. 46, 48149 Münster, Germany

I. Gonzalez-Iulian

Forschungszentrum Jülich GmbH

Institute of Energy and Climate Research: Materials Synthesis and Processing (IEK-1)

Wilhelm-Johnen-Straße, 52428 Jülich, Germany



The ORCID identification number(s) for the author(s) of this article can be found under https://doi.org/10.1002/smll.202104130.

© 2021 The Authors. Small published by Wiley-VCH GmbH. This is an open access article under the terms of the Creative Commons Attribution License, which permits use, distribution and reproduction in any medium, provided the original work is properly cited.

DOI: 10.1002/smll.202104130

exhibit characteristic chemical and physical properties, which can be utilized in different fields of application, such as electrochemical energy storage, electromagnetic interference shielding, CO catalysis, water purification, gas separation, antibacterial agent, and more.[1] The term "MXene" was selected according to the synthesis approach utilizing the parent layered material class as precursor, that is, MAX phases. This class of materials follows the general elemental ratio of  $M_{n+1}AX_n$ , where "M" is a transition metal (e.g., titanium (Ti)), "A" corresponds to a group A element (e.g., aluminum (Al), group IIIA), and "X" is carbon (C) and/or nitrogen (N) in a fixed stoichiometry with n being equal to 1, 2, or 3 (e.g.,  $Ti_3AlC_2$ ). To synthesize MXenes, the "A" layer is removed from the MAX phase, representing the "MX" in MXene and, additionally, the term "ene" was added to show the

structural resemblance between MXenes and graphene. Therefore, the overall stoichiometric ratio of MXenes is limited by its parent MAX phase.<sup>[2]</sup>

HF-containing acidic solutions are usually used for the removal of the "A" element, which can be in form of pure HF acid or in form of in situ formed HF using fluoride salts and a strong acid (e.g., HCl/LiF). [2c-e] The occurrence of electrophilic, surface terminating groups bonded to the transition metal are unavoidable during synthesis and influence the overall physical, chemical and electrochemical properties of the MXene (e.g.,  $\text{Ti}_3\text{AlC}_2 \rightarrow \text{Ti}_3\text{C}_2T_x$ ;  $T_x = \text{F}$ , Cl, O, OH; theoretically: x = 2). Additionally, macroscopic properties, such as particle morphology and specific surface area can be influenced by the synthesis and, therefore, multi-layered, few-layered or single-/mono-layered particles/sheets can be synthesized. Subsequently, the material properties depend on the parent MAX phase morphology, on the chemical etching, and post-treatment procedures (calcination, acid washing, and more). [2c,3]

MXenes can be utilized in the field of electrochemical energy storage (EES) due to their so-called "pseudocapacitive properties". In comparison to "classical" intercalation, insertion or alloying materials, pseudocapacitive materials display both diffusion-limited (redox = Faradaic) and non-diffusion-limited (non-Faradaic) processes. When both processes are present during (dis)charge, pseudocapacitive materials unite the desired properties between high-power density



www.advancedsciencenews.com



and high-energy density for EES applications.<sup>[4]</sup> Pseudocapacitive materials can offer a beneficial compromise between (i) kinetically-limited intercalation or so called "alloying" materials using a redox reaction mechanism with high capacity and (ii) purely capacitive materials, that offer fast charge/discharge, however with low capacities (=charge storage in the electrochemical double layer).<sup>[4]</sup>

Due to rapid development and discovery of various materials, a precise definition of the term "pseudocapacitance" has proven to be challenging, although the underlying physical and electrochemical laws are the same for all the active materials. Usually, the definition is split into three categories: Adsorption, redox, and intercalation pseudocapacitance are defined by the linearity of the extent of the reaction and the potential. Here, the extent of the reaction is defined by Conway as the surface coverage (adsorption), concentration of the oxidant (redox), and the lattice occupancy (intercalation). The linearity regarding the potential manifests electrochemically in a high reversibility during (dis)charge with no mass transfer limitations, which are both desirable properties for LIB cells. [4c,5] Since the presented definition by Conway is not based on an atomistic description of the underlying active material, similarities to other electrochemical phenomena can be expected. Especially the analogy in the definition of the intercalation pseudocapacitance and the solid-solution intercalation mechanism by Aurbach et al.<sup>[6]</sup> is worth mentioning.

MXenes can undergo intercalation-type pseudocapacitance, as alkali cations (e.g., Li<sup>+</sup> in lithium ion batteries, LIB battery configuration)[7] can intercalate between negatively charged layers without any mechanical deformation; charge transfer between MXene host and alkali ion guests can occur.[4] However, for MXenes, the observed reversible capacity is drastically influenced by the surface groups and the type of intercalated species. This is due to the change in the electronic structure of the MXene for different surface groups, since the atomic orbitals of the cations hybridize with the orbitals from the surface groups upon lithiation.[8] Although this atomistic understanding of the electrochemical charge and discharge mechanism of MXenes was established, delaminated MXenes, that is, few- and single-layered, generally show an increase of capacity upon cycling ("activation") and especially multi-layered MXenes exhibit a loss of reversible charge storage in the first cycles ("capacity fade"), which has not been addressed so far.[1c,d,9]

This work aims to shed light on this phenomenon by comparing and exploring the change of the electrochemical and structural properties of few-layered Ti<sub>3</sub>C<sub>2</sub> (f-Ti<sub>3</sub>C<sub>2</sub>) and multilayered Ti<sub>3</sub>C<sub>2</sub> (m-Ti<sub>3</sub>C<sub>2</sub>) when applied as negative electrodes in lithium ion battery (LIB) cells. First, the electrochemical characteristics were analyzed by galvanostatic cycling. Motivated by this investigation, the pseudocapacitive behavior was investigated by cyclic voltammetry and impedance spectroscopy to quantify the electrochemical performance changes occurring upon cycling of the active materials. These electrochemical investigations led to the analysis of the structural properties of multi- and few-layered MXenes in the first cycles via in situ XRD. The synthesis conditions of the Ti<sub>3</sub>C<sub>2</sub> MXenes used in this work are summarized in our previous work, which results in a chemical composition of  $\text{Ti}_3\text{C}_2\text{O}_{1.1}\text{OH}_{0.3}\text{F}_{0.8}$  for m-Ti $_3\text{C}_2$ and Ti<sub>3</sub>C<sub>2</sub>O<sub>1.1</sub>OH<sub>0.3</sub>F<sub>0.8</sub>Cl<sub>0.2</sub> for f-Ti<sub>3</sub>C<sub>2</sub>.<sup>[10]</sup>

#### 2. Results and Discussion

### 2.1. Deciphering the Pseudocapacity of Few- and Multi-Layered MXenes

To shed light on the underlying mechanisms for capacity fade and activation for m-Ti<sub>3</sub>C<sub>2</sub> and f-Ti<sub>3</sub>C<sub>2</sub> MXenes, galvanostatic investigations were conducted, followed by analysis of the differential capacity versus potential profiles to detect significant changes occurring during cycling, as shown in **Figure 1**.

First, f-Ti<sub>3</sub>C<sub>2</sub> exhibits the expected, overall improved electrochemical performance in comparison to its multi-layered counterpart with capacities of 263 mAh g-1 for f-Ti<sub>3</sub>C<sub>2</sub> and 107 mAh g<sup>-1</sup> for m-Ti<sub>3</sub>C<sub>2</sub> after 200 cycles (Figure 1a). This difference was shown by our previous work to be a result of the increased non-diffusion-limited capacity due to the higher surface area of the delaminated MXene.[10] Although already visible in Figure 1a, the capacity fade and MXene-typical activation phenomena are better visible in Figure 1d showing the normalized capacities.[1d,9a,b,11] Here, the relative capacity drops by 32.6% within the five formation cycles for m-Ti<sub>3</sub>C<sub>2</sub> in comparison to only 10% for f-Ti<sub>3</sub>C<sub>2</sub>. Furthermore, the specific delithiation capacity further decreases for m-Ti<sub>3</sub>C<sub>2</sub> until the 80<sup>th</sup> cycle is reached, after which the de-lithiation capacity stabilizes and afterwards increases again. In contrast, f-Ti<sub>3</sub>C<sub>2</sub> also shows a slight capacity fade in the beginning (4%), while the delithiation capacity stabilizes faster (i.e., after 35 cycles). Thereafter, f-Ti<sub>3</sub>C<sub>2</sub> exhibits a significantly steeper increase in capacity than m-Ti<sub>3</sub>C<sub>2</sub>, which results in a capacity gain of almost 10% after 200 cycles (Figure 1d). Additionally, the Coulombic efficiency ( $C_{\text{Eff}}$ ) in the 1st cycle is comparably low for both materials, that is, 61.0% for f-Ti<sub>3</sub>C<sub>2</sub> and 67.7% for m-Ti<sub>3</sub>C<sub>2</sub>. As discussed in our previous work,[10] a higher difference should be expected as the specific surface area significantly increases through delamination, therefore, the irreversible processes occurring for m-Ti<sub>3</sub>C<sub>2</sub> in the 1st cycle originate from a different process than the usual decomposition of the mixed organic carbonate solvent-based electrolytes at the electrode | electrolyte interface.[12]

Due to the distinctive difference between both samples, that is, the low  $C_{\text{Eff}}$  in the formation cycles for both samples but high reversibility for f-Ti<sub>3</sub>C<sub>2</sub> and poor reversibility for m-Ti<sub>3</sub>C<sub>2</sub>, irreversible reactions (e.g., electrolyte decomposition for solid electrolyte interphase (SEI) formation)[13] cannot fully explain the observed phenomena. By calculating the differential capacities of both samples during the five formation cycles (Figure 1b,e) and long-term cycling (Figure 1c,f), the significant loss of reversible capacity for m-Ti<sub>3</sub>C<sub>2</sub> simultaneously occurs with a potential shift of the main redox peak in the de-lithiation (Figure 1b,c). Over the course of 200 cycles, the de-lithiation peak shifts from 0.9 V (6th cycle) to 1.4 V versus Li|Li<sup>+</sup> (200th cycle). Additionally, the specific differential capacity decreases simultaneously with the shift of the potential. In comparison, the same redox peak does not undergo significant change over the course of 200 cycles for f-Ti<sub>3</sub>C<sub>2</sub> (Figure 1e,f). Usually an increase of the de-lithiation potential for a redox process can be assigned to kinetic limitations resulting in overpotentials, which are responsible for the shift of the potential.[14] Additionally, the lithiation redox peak of m-Ti<sub>3</sub>C<sub>2</sub> at 2 V versus Li|Li<sup>+</sup> also

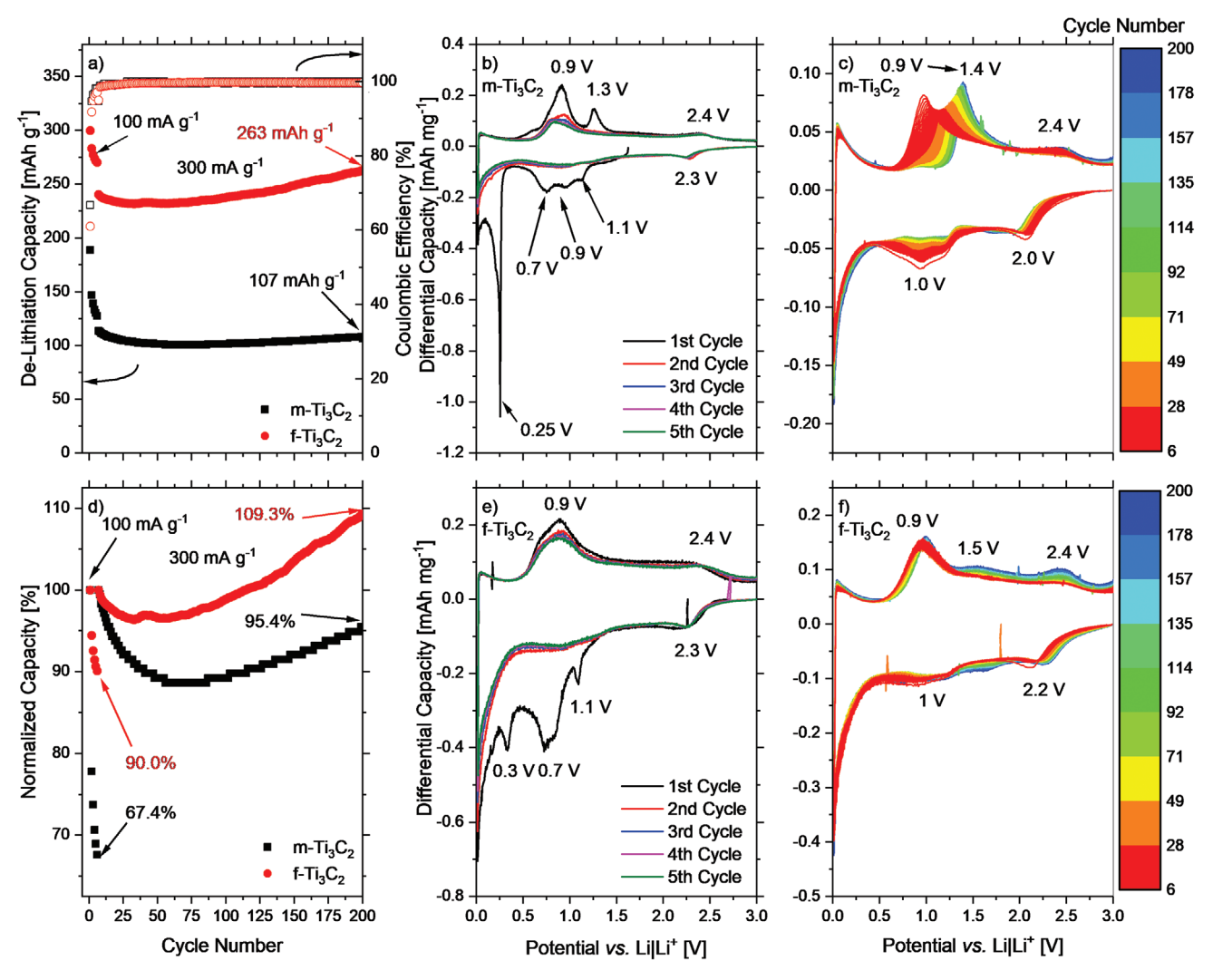


Figure 1. Galvanostatic charge and discharge of m- $Ti_3C_2$  and f- $Ti_3C_2$  and their corresponding differential capacity versus potential profiles. a) Specific de-lithiation capacities during charge/discharge cycling at 100 mA  $g^{-1}$  (formation; five cycles) and 300 mA  $g^{-1}$  (cycling), as labeled in the graphs. d) Normalized capacities, that is, the specific capacities are normalized to the 1st cycle capacity during the formation process and to the 1st cycle of the subsequent regular of cycling process (i.e., the 6th cycle) to illuminate the development of capacity fade during cycling. b,c,e,f) the corresponding differential capacities versus potentials to the galvanostatic cycling for the formation cycles (b,e) and long-term cycling (c,f). m- $Ti_3C_2$  (b,c) and f- $Ti_3C_2$  (e,f). All measurements were performed in MXene || Li metal cells (half-cell setup, three-electrode configuration; potential range: 0.01 and 3 V vs Li|Li<sup>+</sup>) and discussed values are labeled accordingly.

shifts to lower values and the redox peak detected at 1 V versus Li|Li<sup>+</sup> exhibits a significant decrease in intensity in correspondence with the decay of the electrochemical performance. Furthermore, the activation for f-Ti $_3$ C $_2$  visible after the 35th cycle (Figure 1d) can be correlated to a shift of the lithiation redox peak at 2.2 V versus Li|Li<sup>+</sup> to slightly higher values (Figure 1f), indicating reduced kinetic limitations in contrast to m-Ti $_3$ C $_2$ . This behavior also results in an increase of the de-lithiation redox peak located at 2.4 V and an increase of the differential capacity at 1.5 V versus Li|Li<sup>+</sup> for de-lithiation and lithiation, which is clearly visible after the 50th cycle (Figure 1f).

The formation cycle(s) also displays distinctive differences between both samples, which have already been discussed in our previous work. [10] Most notable is the occurrence of a second redox peak during the de-lithiation for m- ${\rm Ti}_3{\rm C}_2$ , which

vanishes after the first cycle (Figure 1b, 1.3V). However, this peak is not detectable for f-Ti $_3$ C $_2$  (Figure 1e). Additionally, the initial lithiation of m-Ti $_3$ C $_2$  is dominated by an irreversible redox peak at 0.25 V (Figure 1b). Such drastic changes in the differential capacity in the first and ongoing cycles indicate that the underlying active material undergoes significant changes in the first cycle. Therefore, the hypothesis arises whether these detected redox peaks in the formation cycle are responsible for the continuous loss of reversible capacity for m-Ti $_3$ C $_2$ .

To investigate this hypothesis electrochemically, the pseudocapacitive behavior was analyzed after the 5th formation cycle and after the 50th and 100th cycles by cyclic voltammetry, because a degradation of the active material should manifest in a change of the pseudocapacitance. Herein, we only focus on the de-lithiation process, as it represents the reversible

reactions and also considers that major changes are influenced by the shift of the redox peak (from 0.9 to 1.4 V vs Li|Li<sup>+</sup>) shown in Figure 1c. The overall pseudocapacitive behavior is evaluated by calculating the "inside" and "outside" surface contribution to the overall capacity and the b-values of the main redox peak values, which are shown in **Figure 2**. Additionally, potentially resolved impedance spectra are used to determine the changes in the charge storage mechanism of the few- and multi-layered MXenes. [8b,15]

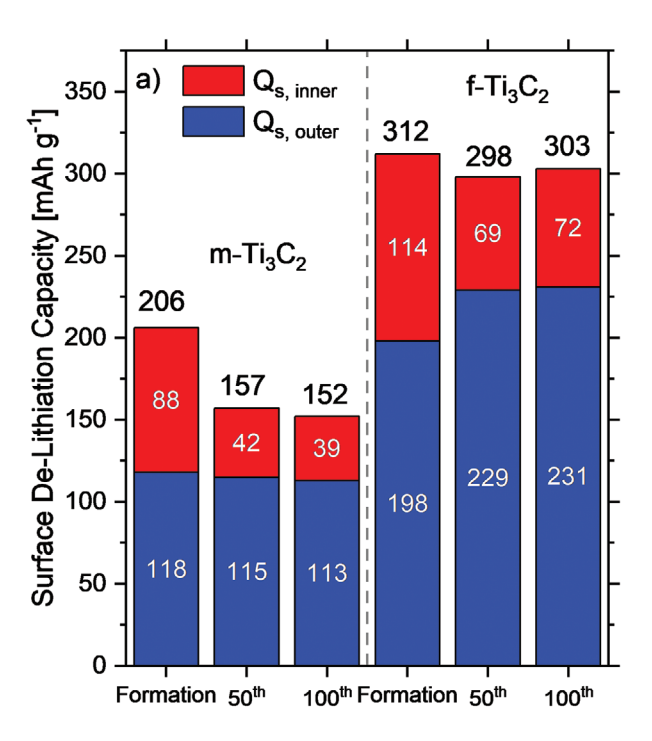
First of all, the overall pseudocapacitive charge storage mechanism of few- and multi-layered MXenes is analyzed by using the method introduced by Trasatti et al., [15e] who categorized the overall capacity into surface-controlled and diffusion-controlled contributions. The total surface-controlled contribution ( $Q_{s,\text{total}}$ ) can even be further split into an "outer" ( $Q_{s,\text{outer}}$ ) and "inner" ( $Q_{s,\text{inner}}$ ) contribution, corresponding to more and less accessible redox active sites, respectively.

As shown in Figure 2a and Figure S1 (Supporting Information), the total surface capacity decreases for m-Ti<sub>3</sub>C<sub>2</sub> from 206 (formation) to 152 mAh g<sup>-1</sup> (100th cycle) in accordance with the galvanostatic investigation, but the outer surface capacity remains nearly constant (118 mAh g-1 after the formation and 113 mAh g<sup>-1</sup> after the 100th cycle). Therefore, only the "inner" surface capacity decreases, which shows that the less accessible redox active sites are electrochemically active upon cycling. In contrast to this, f-Ti<sub>3</sub>C<sub>2</sub> exhibits an overall stable total surface capacity, also with a decreasing "inner" surface capacity (i.e., decrease from 114 mAh g<sup>-1</sup> to 72 mAh g<sup>-1</sup>), which is compensated by an increasing "outer" contribution to the surface capacity. However, the "activation" process, that is, the increase of the de-lithiation capacity during galvanostatic cycling, cannot be explained by these observations. Therefore, and since the capacity is split into the surface contribution and the diffusion contribution, the diffusion contribution must be responsible for the increased de-lithiation capacity leading to the assumption that inactive redox sites are activated upon cycling for f-Ti<sub>3</sub>C<sub>2</sub>.

To investigate this proposed mechanism regarding the potential, the *b*-values of the redox peak at 0.9 V were calculated. Briefly explained, a *b*-value of 0.5 corresponds to a pure diffusion-controlled mechanism and a *b*-value of 1 refers to a pure surface-controlled mechanism (non-diffusion-limited redox process). A *b*-value between 0.5 and 1 corresponds to either a mixture of both contributions or to a finite-length diffusion, as the interpretation is based on the Randles–Ševčík equation, which relies on the principle of a semi-infinite diffusion in the interpretation for redox-active electrodes. [15a-d]

As visible in Figure 2b, both samples exhibit an increase of the b-value, that is, from 0.78 (0.9) for m-Ti $_3$ C $_2$  (f-Ti $_3$ C $_2$ ) after the formation to 0.89 (0.97) after 100 cycles. As explained before, this indicates a more surface-controlled mechanism or a finite-diffusion length for both samples. The b-value for f-Ti $_3$ C $_2$  of almost 1 indicates that the occurring redox reactions are diffusion-independent upon cycling, leading to the observed increase in specific capacity. In contrast to f-Ti $_3$ C $_2$ , the contribution of the diffusion-independent redox reaction increases also for m-Ti $_3$ C $_2$ , but this behavior leads to an overall decrease in specific capacity.

However, since the used electrochemical methods are only powerful in accessing the overall pseudocapacitive behavior, a



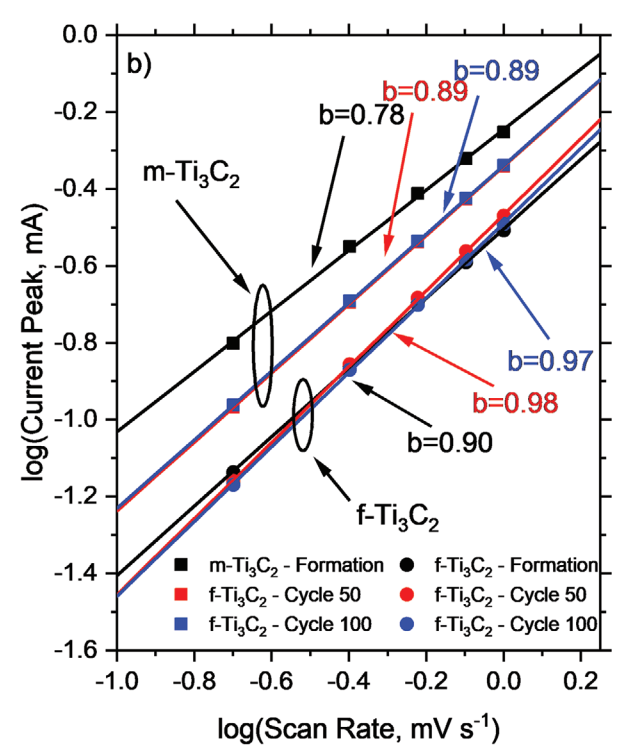


**Figure 2.** Cyclic voltammetry investigations to evaluate the pseudocapacitive behavior of multi- and few-layered  $Ti_3C_2$ . a) Surface de-lithiation capacity  $(Q_s)$  labeled above the bars, which is further split into the "inner" capacity  $(Q_{s,inner})$  and "outer" capacity  $(Q_{s,outer})$ . b) Calculated b-values for the anodic current peak located at 0.9 V versus Li|Li<sup>+</sup> as shown in Figure 1c,f. All cyclic voltammetry measurements were performed after the formation (after the 5th cycle), 50th cycle, and 100th cycle in MXene || Li metal cells (half-cell setup, three-electrode configuration; potential range: 0.01 and 3 V vs Li|Li<sup>+</sup>; scan rates: 0.2, 0.4, 0.6, 0.8, 1, 2, 3, 5 and, 10 mV s<sup>-1</sup>) and discussed values are labeled accordingly.

more distinct and potential resolved analysis is necessary, which was implemented by conducting a step-wise electrochemical impedance spectroscopy (EIS) measurement (every 25 mV), where after a constant voltage step for 10 min, the EIS spectra were measured. The spectra are evaluated by considering the electrode as a pure capacitor and correlating the real part of the capacitance ( $C_{\rm real}$ ) to the phase. Obviously, the response is more complicated for negative electrodes (due to SEI formation, and more) and the applied approach is an oversimplification. Therefore, only low frequencies are examined (5 mHz), and the full data is presented in Figures S2 and S3, Supporting Information. By correlating the calculated capacitance with the phase angle at low frequencies, general statements of the underlying pseudocapacitance are possible in dependence of the potential. [15g-i]

The results are shown in **Figure 3** and, generally, the capacitance can be divided up into four sections for both samples, that is, the first section ranging from 0.1 V to 0.7 V (I), the second one from 0.7 V to 1.3 V (II), the third one from 1.3 V to 2.3 V (III), and the fourth one ranging from 2.3 V to 3 V (IV).

Both MXenes exhibit exponentially decreasing capacitances/capacities in the first section (I), which can be linked to contribution of the conducting agent as well from MXenes, exhibiting enlarged interspace layers due to the co-intercalation of solvent molecules, [3c], a process that is well-known from layered intercalation host materials, such as graphite and TiS<sub>2</sub>. [16] These co-intercalation reactions, in particular their reversibility, are depending on the used solvent. Typically, mixed organic carbonate electrolytes containing ethylene carbonate (EC) do not show a strong tendency for co-intercalation. [12,17] This seems to be fundamentally different for MXenes, as shown here and will be discussed later on.

Additionally, the capacitance in the first section is relatively large in comparison to the capacitance measured in the other three sections for m- $\mathrm{Ti}_3\mathrm{C}_2$  (Figure 3a), which is not the case for f- $\mathrm{Ti}_3\mathrm{C}_2$  (Figure 3b), as also visible in the differential capacity versus potential plot (Figure 1c,f).

Furthermore, the phase is also close to 90° indicating a capacitor-like behavior for m-Ti<sub>3</sub>C<sub>2</sub> and f-Ti<sub>3</sub>C<sub>2</sub> in section (I) and, therefore, no pseudocapacitive behavior. This behavior remains almost the same throughout cycling for both investigated materials. In the second and third section, the capacitance exhibits maxima at 1 V (II) and 1.6 V (III), which both decrease upon cycling for m-Ti<sub>3</sub>C<sub>2</sub> (Figure 3a) and which both increase upon cycling for f-Ti<sub>3</sub>C<sub>2</sub> (Figure 3b). This opposed behavior between both samples also dominates the phase angle, decreasing for m-Ti<sub>3</sub>C<sub>2</sub> from 45°, a diffusion-process, to 30°, more resistorlike processes for the 50th and 100th cycle in the third region (Figure 3a). [8b,14] This behavior can explain the observed shift of the redox peak (from 0.9 to 1.4 V, Figure 1c): since the redox process at 1 V (II) becomes more capacitor-like and therefore loses any pseudocapacitive properties (surface and diffusion processes), we assign this vanishing peak to irreversible reactions occurring during cycling. Additionally, the capacitance maximum in region (III) also decreases, probably due to kinetic-limitations as visible by the shift of the phase toward a more resistor-like behavior, thus, explaining the shift of the redox peak in Figure 1c. Additionally, the capacitor-like behavior from section (I) also extends into region (II) upon cycling. In

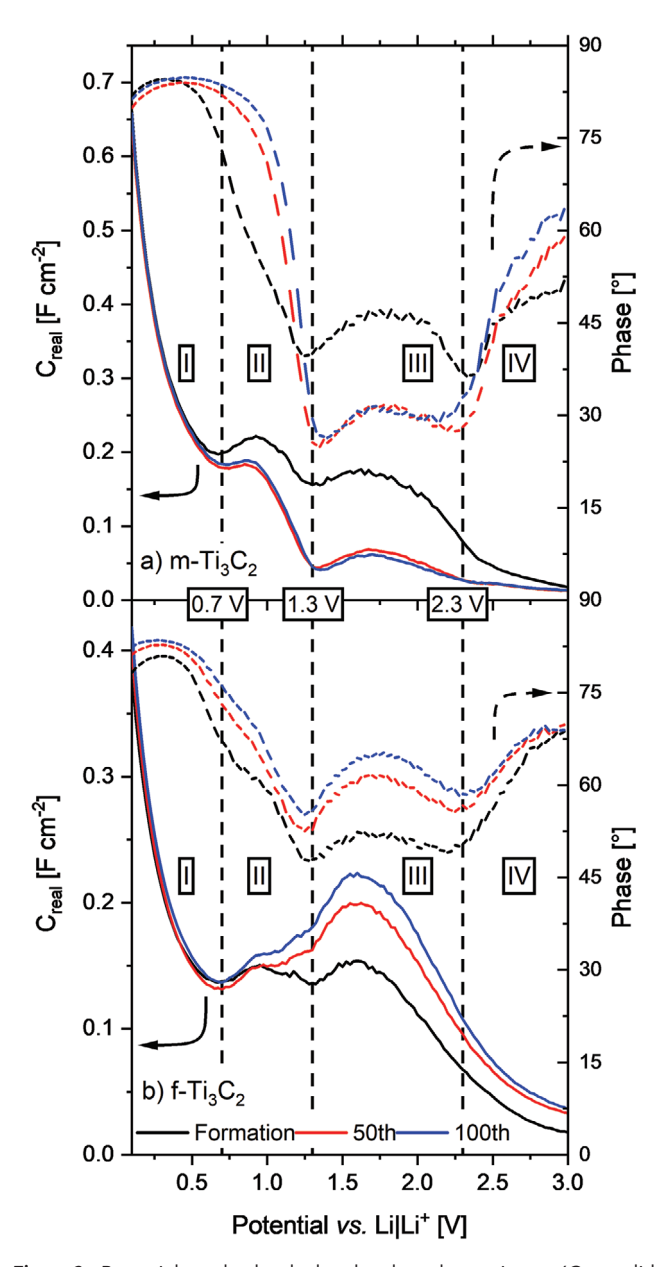


**Figure 3.** Potential-resolved, calculated real areal capacitance ( $C_{\text{real}}$ , solid line) and phase (dashed line) at 5 mHz for a) m-Ti<sub>3</sub>C<sub>2</sub> and b) f-Ti<sub>3</sub>C<sub>2</sub>. The areal capacitances for m-Ti<sub>3</sub>C<sub>2</sub> and f-Ti<sub>3</sub>C<sub>2</sub> can be split into four categories, which are labeled by greek numerals (I–IV) and the potentials are also labeled accordingly. All measurements were performed after the formation, 50th cycle, and 100th cycle in MXene || Li metal cells (half-cell setup, three-electrode configuration; potential range: 0.01 and 3 V vs Li|Li<sup>+</sup>). Complete Nyquist plots, real areal capacitances, and phases are shown in the Figures S2 and S3, Supporting Information.

contrast to this, a gradual increase of capacitance can be seen for f-Ti $_3$ C $_2$  in the third section (Figure 3b) in accordance with the data shown in Figure 1f. Therefore, the activation is mainly driven by an increase of capacitance in the third region (1.3 to 2.3 V), which also exhibits an increasing phase angle, but can still be considered diffusion-limited and, therefore pseudocapacitive process. An additional peak cannot be observed for m-Ti $_3$ C $_2$  and f-Ti $_3$ C $_2$  in the fourth region as detected by

calculating the differential capacities (Figure 1). Nevertheless, the broad maxima in the third region could obscure this peak.

The different electrochemical behavior of both MXenes revealed above leads to the hypothesis that the active material has to undergo significant structural changes, especially within the first cycle.

## 2.2. Investigating the Structural Changes of Few- and Multi-Layered ${\rm Ti_3C_2}$

Therefore, the structural properties of the few- and multilayered MXenes are systematically examined and evaluated via in situ XRD studies for the first three cycles, as shown in Figure 4. Both samples exhibit different "starting"  $2\theta$  angles as measured during the open circuit voltage (OCV), which is  $9.2^{\circ}$  for m-Ti<sub>3</sub>C<sub>2</sub> (Figure 4a) and  $8.4^{\circ}$  for f-Ti<sub>3</sub>C<sub>2</sub> (Figure 4b). This difference shrinks as the active material is lithiated for the first time since m-Ti<sub>3</sub>C<sub>2</sub> shifts to lower 2 theta angles (1.2 V/8.7°) and f-Ti<sub>3</sub>C<sub>2</sub> (1.2 V/8.4°) remains constant. After reaching a cell voltage of 0.8 V, m-Ti<sub>3</sub>C<sub>2</sub> exhibits a broadening due to a reflection emerging at even lower  $2\theta$  angles (0.8 V/8.1°), which continues until a voltage of 0.3 V is reached (Figure 4a). Nevertheless, the aforementioned reflection (1.2 V/8.7°) does decrease in intensity for m-Ti<sub>3</sub>C<sub>2</sub> but is still visible until a voltage of 0.3 V is reached. Within the same voltage range, a shift to  $7.8^{\circ}$  (20) can be observed for f-Ti<sub>3</sub>C<sub>2</sub> until a voltage of 0.3 V is reached, like m-Ti<sub>3</sub>C<sub>2</sub>. Therefore, an alignment in the  $2\theta$  angles between both samples is established, again. However, as the lithiation continues and the cell voltage drops below 0.3 V, m-Ti<sub>3</sub>C<sub>2</sub> undergoes significant structural changes as the interspace layer is increased shown by the shift of the (002) reflection to 7.2° (20) for m-Ti<sub>3</sub>C<sub>2</sub> (Figure 4a), which is like the shift of the same reflection for f-Ti<sub>3</sub>C<sub>2</sub> (0.01 V/7.1°).

Additionally, a new reflection also emerges at 0.3 V for both samples at 5.8° ( $2\theta$ ), indicating a permanent change to the overall structure of f-Ti<sub>3</sub>C<sub>2</sub> and m-Ti<sub>3</sub>C<sub>2</sub>. Therefore, the unidentified redox peak, that is, at 0.25 V (Figure 1b), is accompanied by structural changes occurring to the active material, which is highly likely due to the co-intercalation solvent molecules. [3c]

The shift of the 002 (f-Ti<sub>3</sub>C<sub>2</sub>, Figure 4b) is accompanied by an increase in intensity, which is not expected as for acidic washed samples, no turbostratic ordering should be observed, as shown by our previous work.<sup>[3c]</sup> Nevertheless, the synthesis of the precursor and the MXene is different between this work and our previous work, which has been shown to significantly influence the electrochemical behavior and is also shown by the fact that an additional reflection is observable upon lithiation (Figure 3b, f-Ti<sub>3</sub>C<sub>2</sub>, 5.8° (2 $\theta$ )). Furthermore, by comparing the intensity of the (002) reflection of f-Ti<sub>3</sub>C<sub>2</sub> measured during OCV and in the highest lithiated state (Figure 4b), the ordering is not as significant as for samples investigated in our previous work.[3c] Nevertheless, this difference shows the necessity and importance of further investigations as a clear, atomistic understanding is necessary to explain the corresponding electrochemical performance phenomena.

The drastic shift of the (002) reflection for m-Ti $_3$ C $_2$  is reversible in the first cycle as the  $2\theta$  angle (0.01 V /  $7.2^{\circ}$ ) increases to  $7.9^{\circ}$  (1.0 V) and no loss of long-range ordering for this reflection

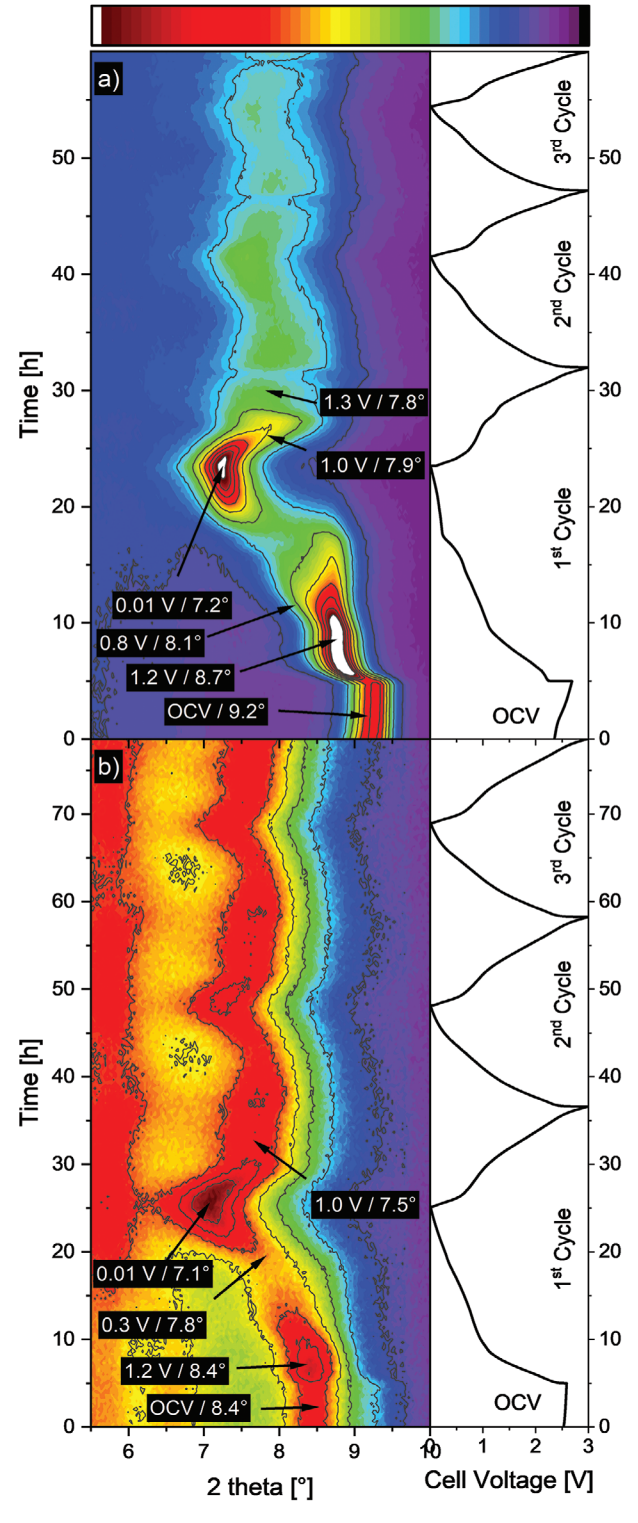


**Figure 4.** In situ XRD of a) m-Ti $_3C_2$  and b) f-Ti $_3C_2$  for the first three charge/discharge cycles. Left: The (002) reflections of the investigated MXenes ranging from high intensity (red; arb. units) to low intensity (purple). The changes occurring in the first cycle are labeled according to voltage / 2 theta angle. Right: Cell voltage plotted against the time of the in situ XRD investigation for the MXene  $\parallel$  Li metal cells (two-electrode configuration; voltage range: 0.01–3 V; specific current: 20 mA g $^{-1}$ ). The corresponding cycles are labeled accordingly.

is detectable (Figure 4a). Future studies must show whether this behavior can be electrochemically reversible beyond the first cycle, which - if shown - would open new possibilities to implement MXenes into LIB cells. Thereby, the overall energy density could be increased due to a decrease of the overall operating voltage of the negative electrode material. Furthermore, f-Ti<sub>3</sub>C<sub>2</sub> also shows an increase to 7.5° (2θ) upon de-lithiation (Figure 4b), which does not change until the cut-off voltage of 3 V is reached (1.0 V/7.5°). In contrast, the (002) reflection of m-Ti<sub>3</sub>C<sub>2</sub> exhibits a loss of long-range ordering as the reflection is significantly broadened and a loss of intensity is detected (1.3 V/7.8°) upon further de-lithiation (Figure 4a). Furthermore, this behavior is not reversible as visible by the changes occurring in the second and third cycle, in contrast to f-Ti<sub>3</sub>C<sub>2</sub>. This behavior explains the occurrence of the second redox peak for m-Ti<sub>3</sub>C<sub>2</sub> observed in the first cycle during galvanostatic cycling (Figure 1b), since m-Ti<sub>3</sub>C<sub>2</sub> does undergo a phase change at this particular potential during de-lithiation. Therefore, both MXenes exhibit co-intercalation of solvent molecules, leading to significant structural changes for m-Ti<sub>3</sub>C<sub>2</sub>, which are not reversible and therefore the origin of the capacity fade. In contrast, the behavior of f-Ti<sub>3</sub>C<sub>2</sub> is highly reversible throughout cycling and a newly emerged reflection (at  $5.8^{\circ}$  (2 $\theta$ )) exhibits reversibility, which might be responsible for the activation observed upon further cycling.

#### 3. Conclusion

In conclusion, this study aims to shed light on the "activation" process and capacity fading mechanisms of multi- and fewlayered MXenes, which is achieved by electrochemical and analytical means. First, galvanostatic investigations reveal a contrary electrochemical performance for m-Ti<sub>3</sub>C<sub>2</sub> and f-Ti<sub>3</sub>C<sub>2</sub>, whereas m-Ti<sub>3</sub>C<sub>2</sub> exhibits detrimental capacity fading in the first cycles, which continues until the 80th cycle. On the other hand, f-Ti<sub>3</sub>C<sub>2</sub> exhibits only negligible capacity fading in the first cycles in comparison to m-Ti<sub>3</sub>C<sub>2</sub>, after which an "activation" process is visible, that is, an increase in capacity upon cycling. This behavior also results in a significant shift of main de-lithiation redox peak, which was identified by analysis of the differential capacities. Furthermore, the low initial  $C_{\rm Eff}$ for m-Ti<sub>3</sub>C<sub>2</sub> and f-Ti<sub>3</sub>C<sub>2</sub> leads to the hypothesis that the active material must undergo significant changes. Motivated by these results, the pseudocapacitive behavior was investigated by cyclic voltammetry (CV) and EIS. First, the CV measurements reveal that the decrease in capacity can be correlated to a decrease in the surface capacity, which was further deduced to the loss of the "inner" surface-capacity contribution (less accessible), while the "outer" surface capacity remains constant. Although, a similar behavior (decrease of the "inner" surface capacity) is observed for f-Ti<sub>3</sub>C<sub>2</sub>, the decrease of the inner surface capacity is compensated by an increase of outersurface capacity. Therefore, we conclude that electrochemical cycling leads to a transformation (activation) of less accessible ("inner") redox active sites to more accessible ("outer") redox active sites. However, for m-Ti<sub>3</sub>C<sub>2</sub>, no transformation is visible and a loss of the total and "outer" surface capacity can be detected.

This conclusion leads to the potential-resolved investigation of the change of pseudocapacitive behavior upon cycling. Here, the calculated de-lithiation capacitance was split into four distinctive regions, dominated by two distinctive maxima present at 0.9 and 1.6 V versus Li|Li<sup>+</sup>. The capacity fade and shift of the main redox peak of m-Ti<sub>3</sub>C<sub>2</sub> are due to a loss of the pseudocapacitive behavior of the first maxima and a kinetic limitation of the second maxima. In contrast to this, f-Ti<sub>3</sub>C<sub>2</sub> exhibits an increase in capacitance for the second maxima in accordance with the galvanostatic investigation, while still showing a pseudocapacitive behavior.

These vastly different electrochemical findings lead to the hypothesis that the structure of the active material must undergo significant changes, especially for m-Ti<sub>3</sub>C<sub>2</sub>. In situ XRD investigations revealed the co-intercalation of solvent molecules, which induces irreversible structural changes for m-Ti<sub>3</sub>C<sub>2</sub>, which are highly likely the reason for capacity fading. However, the loss of long-range ordering during de-lithiation (1.3 V) could be observed, raising the hypothesis that solvent co-intercalation or the reaction between the solvent molecule and the MXene are able to retain the structure, which in turn could lead to new structural designs of multi-layered MXenes. In contrast to that, f-Ti<sub>3</sub>C<sub>2</sub> does not show an irreversible change to its overall structure. Additionally, a new reflection emerges, showing a larger interspace layer. This reflection might be responsible for the activation observed upon further cycling as the large interspace layer could lead to an increased accessibility of redox active site.

Summarizing the mechanism (see Figure 5) for m-Ti<sub>3</sub>C<sub>2</sub>, the co-intercalation of lithium ions together with solvent molecules within the first cycle leads to a loss of long-range order of the MXene host, which in turn manifests itself in the change of electrochemical behavior, as a loss of surface de-lithiation capacity is observable. This loss can be further deduced to a continuous loss of "less accessible" surface redox active sites, therefore we hypothesize, that the loss of long-range ordering of m-Ti<sub>3</sub>C<sub>2</sub> inhibits the further reversible storage of lithium cations at these redox sites. This leads to the observable capacity fade and then capacity stagnation or slow capacity increase. Summarizing the mechanism for f-Ti<sub>3</sub>C<sub>2</sub>, first, a similar cointercalation occurs within the first cycle, which also leads to a loss of the less "accessible surface" redox active sites, but contrary to m-Ti<sub>3</sub>C<sub>2</sub>, the "accessible surface" capacity increases, indicating a transformation. This transformation leads to a rather noteworthy capacity increase, which can be regarded as "activation".

Although the co-intercalation phenomenon is well-known from layered electrode materials (in particular from graphite anodes, as discussed above), the formation of an SEI on the negative electrode usually prevents the co-intercalation in organic carbonate solvent electrolytes, which is clearly not the case for MXene. Additionally, a co-intercalation and at least partially reversible charge transfer is clearly visible for both MXene materials, which is very similar to the co-intercalation behavior of graphite with DMSO based electrolytes.<sup>[18]</sup>

Therefore, future works should focus on the kinetic stability of the co-intercalated species and especially their solid and gaseous reduction products of multi- and few-layered MXenes. The investigation of EC-, PC-, and DMSO-based electrolytes could be

www.advancedsciencenews.com

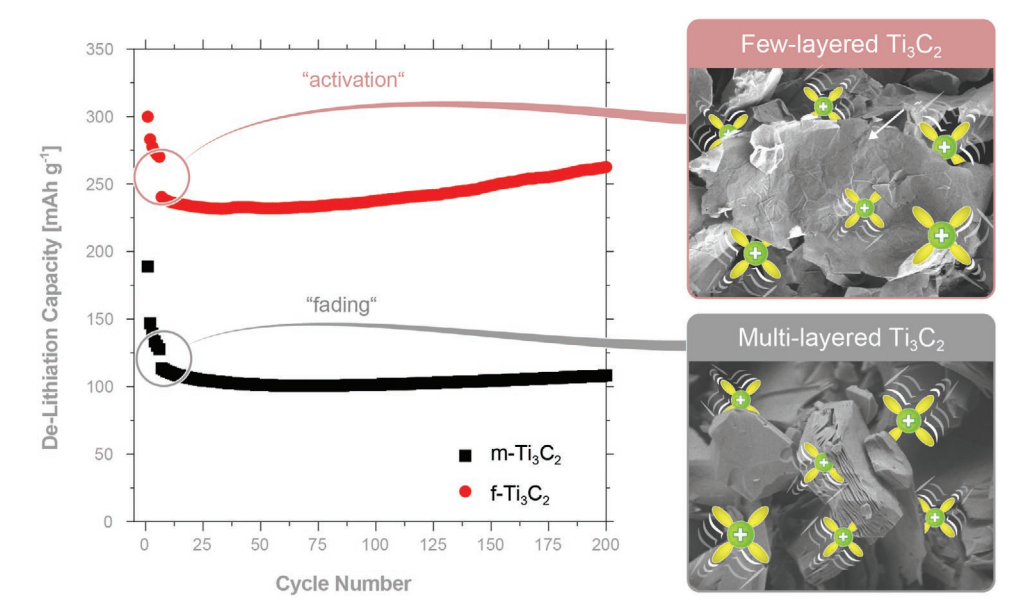


Figure 5. Schematic drawing showing the solvent co-intercalation-induced activation and capacity fade mechanism of few-/multi-layered MXenes.

of great interest, as for graphite, these solvents show fast, moderate, and slow decomposition rates, respectively, which leads to vastly different electrochemical behaviors. Additionally, the influence of the surface termination on the presented storage mechanism has to be deciphered to further improve the electrochemical stability of titanium-based MXenes for the use in LIBs.

#### 4. Experimental Section

Materials and Electrode Preparation: The MAX phase and Ti<sub>3</sub>C<sub>2</sub> MXenes were synthesized according to our previous publication. [10] The composite electrodes consisted of 80 wt% active material (m-Ti<sub>3</sub>C<sub>2</sub> or f-Ti<sub>3</sub>C<sub>2</sub>), 10 wt% polyvinylidene difluoride (PVdF; Solef 5130; Solvay) as binder and 10 wt% of conductive agent (C-nergy Super C65 carbon black; Imerys Graphite & Carbon), while N-Methyl-2-pyrrolidone (NMP; anhydrous; 99.5%; Sigma-Aldrich) was used as processing solvent. The electrode paste was stirred for 24 h inside an Ar-filled glovebox. Afterward, the paste was cast onto a dendritic copper foil (Schlenk; thickness: 20  $\mu$ m; purity of >99.9%) using a standard doctor-blade technique in ambient air. A blade gap of 50  $\mu m$  was chosen, so that the electrodes exhibited an active mass loading of  $\approx 0.5-0.6$  mg cm<sup>-2</sup>. The electrode sheets were quickly moved to a vacuum oven and dried at reduced pressure for 12 h at room temperature. Circular electrodes with a diameter of 18 mm were punched out and dried at 80 °C under reduced pressure for 24 h.

*Electrochemical Characterization*: All electrochemical investigations were carried out in a half-cell setup (three-electrode configuration; EL-Cell) by control of the working electrode (WE, Ø18 mm) potential via the reference electrode (RE). Li metal (Albemarle; battery grade) was used as counter electrode (CE, Ø18 mm) and RE. A Ø13 mm separator (Freudenberg, FS 2226) was used, which was soaked with 120 μL of 1M LiPF $_6$  EC:EMC (3:7 by weight; BASF, battery grade).

Charge/discharge cycling was carried out on a VMP multichannel constant voltage–constant current system (Bio-Logic Science Instruments) at 20 °C in a WE potential range between 0.01 and 3 V versus Li|Li<sup>+</sup>. The specific currents for the galvanostatic cycling are labeled in the designated graphs. Cyclic voltammetry experiments were conducted by using scan rates of 0.2, 0.4, 0.6, 0.8, 1, 2, 3, 5, and 10 mV s<sup>-1</sup>.

To measure the AC impedance, stepped potential electrochemical impedance spectroscopy (EIS) was applied in intervals of 25 mV (10 min holding time, 0.01–3 vs Li|Li<sup>+</sup>), with an amplitude of 10 mV in a frequency range of 100kHz to 5 mHz. The impedance measurements as well as the potentiostatic measurements were conducted after the formation cycles (five cycles) as well as after the 50th and 100th cycle.

In Situ X-Ray Diffraction Studies: In situ XRD analyses of the active materials upon galvanostatic cycling were carried out using a selfdesigned in situ cell (two-electrode configuration), as described previously. [2] The electrode paste preparation was carried out as before, and subsequently, the paste was cast homogeneously onto a beryllium (Be) disk (thickness of 250 μm, Brush Wellman). Li metal was used as CE. A Whatman glass fiber separator (grade GF/D) was used with 400  $\mu L$  of the same electrolyte. The cell was cycled with a constant current of 20 mA g<sup>-1</sup> at a VMP multichannel constant voltage-constant current system (Bio-Logic Science Instruments) in a voltage range of 0.01 and 3 V for three cycles. Before cycling, the cell was equilibrated using an open circuit voltage (OCV) step of 6 h. XRD investigations were conducted only in the range from 5° to 20° with a step size of 0.03° and a dwell time of 1.8 s. Before conducting the experiment, a full diffraction pattern was recorded from 5° to 80° with a step size of 0.03° and a dwell time of 2 s, from which the Be (110) reflection was used for referencing the patterns.

#### **Supporting Information**

Supporting Information is available from the Wiley Online Library or from the author.

#### Acknowledgements

The authors thank the Ministry of Economic Affairs, Innovation, Digitalization and Energy of the State of North Rhine-Westphalia (MWIDE) for funding this work in the project "GrEEn" (313-W044A). Andre Bar and Melina Poll are acknowledged for his graphical and her synthesis support, respectively.

Open access funding enabled and organized by Projekt DEAL.

www.advancedsciencenews.com



#### **Conflict of Interest**

The authors declare no conflict of interest.

#### **Data Availability Statement**

The data that support the findings of this study are available from the corresponding author upon reasonable request.

#### **Keywords**

in situ XRD, lithium ion batteries, MXenes, solvent co-intercalation,  $Ti_3C_2T_x$ 

Received: August 3, 2021 Published online: October 11, 2021

- [1] a) M. Naguib, M. Kurtoglu, V. Presser, J. Lu, J. Niu, M. Heon, L. Hultman, Y. Gogotsi, M. W. Barsoum, Adv. Mater. 2011, 23, 4248;
  b) Y. Xie, Y. Dall'Agnese, M. Naguib, Y. Gogotsi, M. W. Barsoum, H. L. Zhuang, P. R. C. Kent, ACS Nano 2014, 8, 9606; c) B. Anasori, M. R. Lukatskaya, Y. Gogotsi, Nat. Rev. Mater. 2017, 2, 16098;
  d) M. Naguib, J. Come, B. Dyatkin, V. Presser, P.-L. Taberna, P. Simon, M. W. Barsoum, Y. Gogotsi, Electrochem. Commun. 2012, 16, 61;
  e) J. Pang, R. G. Mendes, A. Bachmatiuk, L. Zhao, H. Q. Ta, T. Gemming, H. Liu, Z. Liu, M. H. Rummeli, Chem. Soc. Rev. 2019, 48, 72.
- [2] a) M. W. Barsoum, MAX Phases: Properties Of Machinable Ternary Carbides and Nitrides, Wiley-VCH, Weinheim, Germany 2013;
  b) J. Gonzalez-Julian, J. Am. Ceram. Soc. 2020, 104, 659;
  c) M. Alhabeb, K. Maleski, B. Anasori, P. Lelyukh, L. Clark, S. Sin, Y. Gogotsi, Chem. Mater. 2017, 29, 7633;
  d) X. Chen, Y. Zhu, M. Zhang, J. Sui, W. Peng, Y. Li, G. Zhang, F. Zhang, X. Fan, ACS Nano 2019, 13, 9449;
  e) S. Kajiyama, L. Szabova, H. linuma, A. Sugahara, K. Gotoh, K. Sodeyama, Y. Tateyama, M. Okubo, A. Yamada, Adv. Energy Mater. 2017, 7, 1601873.
- [3] a) O. Mashtalir, M. Naguib, V. N. Mochalin, Y. Dall'Agnese, M. Heon, M. W. Barsoum, Y. Gogotsi, Nat. Commun. 2013, 4, 1716;
  b) M. Naguib, O. Mashtalir, J. Carle, V. Presser, J. Lu, L. Hultman, Y. Gogotsi, M. W. Barsoum, ACS Nano 2012, 6, 1322;
  c) P. Bärmann, R. Nölle, V. Siozios, M. Ruttert, O. Guillon, M. Winter, J. Gonzalez-Julian, T. Placke, ACS Nano 2021, 15, 3295.
- [4] a) V. Augustyn, J. Come, M. A. Lowe, J. W. Kim, P.-L. Taberna, S. H. Tolbert, H. D. Abruña, P. Simon, B. Dunn, *Nat. Mater.* 2013, 12, 518; b) V. Augustyn, P. Simon, B. Dunn, *Energy Environ. Sci.* 2014, 7, 1597; c) B. E. Conway, *J. Electrochem. Soc.* 1991, 138, 1539; d) P. Simon, Y. Gogotsi, B. Dunn, *Science* 2014, 343, 1210.
- [5] a) B. E. Conway, Electrochim. Acta 1993, 38, 1249; b) B. E. Conway, Electrochemical Supercapacitors: Scientific Fundamentals and Technological Applications, Springer Science & Business Media, Berlin 2013; c) B. E. Conway, H. Angerstein-Kozlowska, Acc. Chem.

- Res. 2002, 14, 49; d) B. E. Conway, E. Gileadi, Trans. Faraday Soc. 1962, 58, 2493; e) S. Hadži-Jordanov, H. Angerstein-Kozlowska, B. E. Conway, J. Electroanal. Chem. Interfacial Electrochem. 1975, 60, 359; f) S. Hadži-Jordanov, H. Angerstein-Kozlowska, M. Vukovič, B. E. Conway, J. Electrochem. Soc. 1978, 125, 1471.
- [6] M. D. Levi, D. Aurbach, Electrochim. Acta 1999, 45, 167.
- [7] a) R. Schmuch, R. Wagner, G. Hörpel, T. Placke, M. Winter, *Nat. Energy* **2018**, *3*, 267; b) M. Winter, B. Barnett, K. Xu, *Chem. Rev.* **2018**, *118*, 11433.
- [8] a) M. Okubo, A. Sugahara, S. Kajiyama, A. Yamada, Acc. Chem. Res. 2018, 51, 591; b) S. Fleischmann, J. B. Mitchell, R. Wang, C. Zhan, D.-e. Jiang, V. Presser, V. Augustyn, Chem. Rev. 2020, 120, 6738.
- [9] a) R. Cheng, T. Hu, H. Zhang, C. Wang, M. Hu, J. Yang, C. Cui, T. Guang, C. Li, C. Shi, P. Hou, X. Wang, J. Phys. Chem. C 2019, 123, 1099; b) D. Xiong, X. Li, Z. Bai, S. Lu, Small 2018, 14, 1703419; c) D. Sun, M. Wang, Z. Li, G. Fan, L.-Z. Fan, A. Zhou, Electrochem. Commun. 2014, 47, 80; d) C. E. Ren, M.-Q. Zhao, T. Makaryan, J. Halim, M. Boota, S. Kota, B. Anasori, M. W. Barsoum, Y. Gogotsi, ChemElectroChem 2016, 3, 689; e) G. Zeng, N. Shi, M. Hess, X. Chen, W. Cheng, T. Fan, M. Niederberger, ACS Nano 2015, 9, 4227.
- [10] P. Bärmann, L. Haneke, J. Wrogemann, O. Guillon, T. Placke, J. Gonzalez-Julian, ACS Appl. Mater. Interfaces 2021, 13, 26074.
- [11] X. Zhang, Z. Zhang, Z. Zhou, J. Energy Chem. 2018, 27, 73.
- [12] a) K. Xu, Chem. Rev. 2004, 104, 4303; b) K. Xu, Chem. Rev. 2014, 114, 11503
- [13] M. Winter, Z. Phys. Chem. 2009, 223, 1395.
- [14] A. J. Bard, L. R. Faulkner, Electrochemical Methods: Fundamentals and Applications, John Wiley & Sons, New York, NY 2000.
- [15] a) K. Aoki, K. Tokuda, H. Matsuda, J. Electroanal. Chem. Interfacial Electrochem. 1984, 160, 33; b) J. S. Ko, M. B. Sassin, D. R. Rolison, J. W. Long, Electrochim. Acta 2018, 275, 225; c) H. Lindström, S. Södergren, A. Solbrand, H. Rensmo, J. Hjelm, A. Hagfeldt, S.-E. Lindquist, J. Phys. Chem. B 1997, 101, 7717; d) T. C. Liu, W. G. Pell, B. E. Conway, S. L. Roberson, J. Electrochem. Soc. 1998, 145, 1882; e) S. Ardizzone, G. Fregonara, S. Trasatti, Electrochim. Acta 1990, 35, 263; f) D. Baronetto, N. Krstajić, S. Trasatti, Electrochim. Acta 1994, 39, 2359; g) L. Bai, B. E. Conway, J. Electrochem. Soc. 1991, 138, 2897; h) L. Bai, B. E. Conway, Electrochim. Acta 1993, 38, 1803; i) J. S. Ko, C.-H. Lai, J. W. Long, D. R. Rolison, B. Dunn, J. N. Weker, ACS Appl. Mater. Interfaces 2020, 12, 14071; j) P. L. Taberna, P. Simon, J. F. Fauvarque, J. Electrochem. Soc. 2003, 150, A292.
- [16] a) J. R. Dahn, M. A. Py, R. R. Haering, Can. J. Phys. 1982, 60, 307;
  b) M. R. Wagner, J. H. Albering, K. C. Moeller, J. O. Besenhard, M. Winter, Electrochem. Commun. 2005, 7, 947;
  c) M. R. Wagner, P. R. Raimann, A. Trifonova, K. C. Moeller, J. O. Besenhard, M. Winter, Electrochem. Solid-State Lett. 2004, 7, A201.
- [17] a) I. Cekic-Laskovic, N. von Aspern, L. Imholt, S. Kaymaksiz,
  K. Oldiges, B. R. Rad, M. Winter, *Top. Curr. Chem.* 2017, 375, 37;
  b) M. Winter, G. H. Wrodnigg, J. r. O. Besenhard, W. Biberacher,
  P. Novák, *J. Electrochem. Soc.* 2000, 147, 2427.
- [18] a) J. O. Besenhard, Carbon 1976, 14, 111; b) S. Maruyama,
   T. Fukutsuka, K. Miyazaki, T. Abe, Electrochim. Acta 2018, 265, 41.